ACS OMEGA

Open Access

http://pubs.acs.org/journal/acsodf

Article

Development of V_2O_3 Nanostructures for Alkali Metal Ion Batteries: A Novel Approach through Mild Metal Vapor Reduction and Interface Engineering

Liang Liu, Yichi Zhang, Yun Wang, Limei Wang,* and Jian Liu

Cite This: *ACS Omega* 2024, 9, 33815−33825

Read Online

ACCESS | Metrics & More | Article Recommendations | Supporting Information

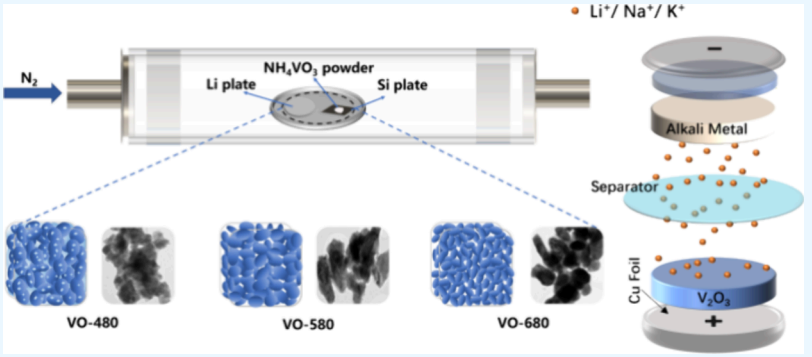

ABSTRACT: V_2O_3 has been extensively researched as a battery electrode material due to its ample reserves and high theoretical capacity. However, the synthesis of valence-sensitive V_2O_3 presents technical challenges as it requires a strict combination of high-temperature treatment and a narrow range of oxygen partial pressures. This study proposes a gentle Li vapor-assisted thermal reduction method to synthesize pure-phase V_2O_3 at a relatively low temperature of 480 °C without any hazardous gases. It has been discovered that reducing the temperature also improves the specific surface area of the nanoto-mesoscale hierarchical structures and enhances the reactive sites between their secondary grains. These advantages enable the V_2O_3 micronano particles to store higher levels of Li^+, Na^+, and K^+, increase ionic transport, and tolerate volume expansion. It demonstrates a significant capacity of 767 mA h g^{-1} in lithium-ion batteries, 393 mA h g^{-1} in sodium-ion batteries, and 209 mA h g^{-1} in potassium-ion batteries. It has also been discovered that the crystal structure of V_2O_3 is easily adjustable by varying the synthesis temperature, which significantly affects the electrochemical storage mechanism. The V_2O_3 synthesized at 480 °C with low crystallinity exhibits a notable intercalation reaction, facilitating the electrochemical kinetics of reversible insertion/extraction of Li^+, Na^+, and K^+. In contrast, the highly crystalline sample synthesized at 580 °C displays pseudocapacitance behavior instead of an intercalation reaction. The highly crystalline sample synthesized at 680 °C exhibits a thorough pseudocapacitance reaction possessing the capacitive functionality for the electrochemical storage of Na^+ or K^+ with larger ion radii. This study describes a new synthesis strategy and rational modification of vanadium-based electrodes for alkali metal ion batteries, leading to the development of reasonably priced rechargeable battery systems with applications extending beyond lithium-ion batteries.

1. INTRODUCTION

There is a strong demand for environmentally friendly and sustainable energy supplies, such as hydropower, solar, and wind resources, to address the depletion of fossil fuels and related environmental problems. The above renewable energy resources are intermittent, causing inconvenience and low efficiency between energy collection and utilization.[1] Rechargeable batteries are considered one of the best energy storage media to regulate these intermittent energy resources.[2] Lithium-ion batteries (LIBs) dominate the rechargeable battery market due to their flexible shape and size, high energy density, and long cycle life.[3−5] The global lithium reserves are limited and geographically restricted to specific areas. It remains controversial whether lithium reserves can meet the rapidly growing demand for large-scale applications of electric vehicles and energy storage power plants,[6] so the other alkali elements, such as sodium (Na) and potassium (K), are attracting the attention of researchers. The Na and K resources are not only available in large quantities at low cost

Received: April 9, 2024
Revised: July 20, 2024
Accepted: July 23, 2024
Published: July 27, 2024

Scheme 1. Lithium Vapor-Assisted Thermal Reduction Synthesis of V_2O_3 Hierarchical Structures with the Tunable Nanostructure

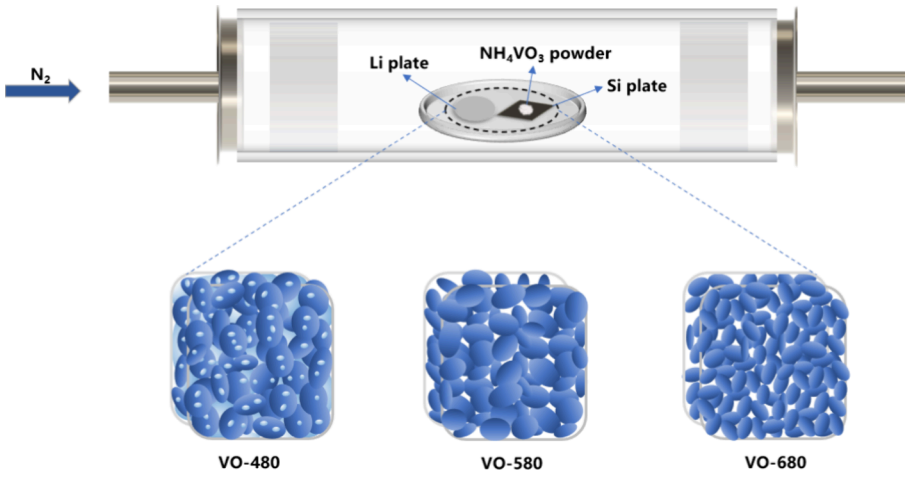

but also evenly distributed around the world.[1,7,8] In addition, sodium-ion batteries (SIBs) and potassium-ion batteries (PIBs) have similar chemical properties and storage mechanisms, wherein the monovalent alkali cations (Na^+ or K^+) reversibly intercalate and deintercalate between layered positive and negative electrodes during the charging and discharging processes. In addition, the mature manufacturing process for commercial LIBs could be readily applied to SIBs and PIBs in the short term.

Compared with Li^+, Na^+, and K^+ have heavier atomic weights and larger ionic radii, resulting in lower theoretical specific capacitance and slower sodiation/potassiation kinetics.[9] Recently, vanadium-based materials have been intensively studied because they exhibit good Na^+/ K^+ storage capability and undergo multielectron reactions due to their rich redox couples.[10,11] Among them, V_2O_3 has been studied due to its natural abundance and low toxicity.[12] Also, the tunneled structure in V_2O_3 promotes the host of large guest atoms of sodium, potassium, and lithium ions.[13−16] Their relatively high specific capacities are attributed to the multistep reduction reaction, meaning that 1 mol of active material can provide several times $n \times 1$ mol of electron transfer.[17] Another fundamental challenge of V_2O_3 is its complex preparation process, which mainly relies on the gas reduction method. However, the abundant oxide forms and polymorphism in vanadium oxides require the rigid synergistic effects of high-temperature treatment and a narrow range of oxygen partial pressures, especially for low-valent vanadium oxide.[13] The low-valent V_2O_3 (with the V-reduced state +3) is commonly synthesized by a solid-state reaction by reducing the cheap high-valent V-based (+5 or +4) starting materials. For example, spherical V_2O_3 powders with an average particle size of 9.5 μm were synthesized by reducing V_2O_5 obtained by evaporative decomposition of solution in H_2 atmosphere at 850 °C for 6 h.[18] Kittaka et al. prepared the spherical V_2O_3 particles of about 10 μm by explosive decomposition of the starting material composed of higher-valence metal ions of V_2O_5 in O_2-H_2 flame fusion at 2000 °C.[19] However, only micrometer-sized powders were obtained by the above methods. Recently, there have been a few techniques to prepare V_2O_3 by inheriting the nano precursor. V_2O_3 nanorods were converted from the metastable VO_2(B) nanorods by a reduction in 5% H_2: 95% N_2 at 600 °C for 3 h.[20]

The high-temperature synthesis of V_2O_3 through gas reduction can cause stress and internal diffusion, complicating the regulation of resulting nanostructures.[21] Additionally, it leads to nonstoichiometric and inhomogeneous properties, as altering reaction parameters may introduce impurities with mixed V-ion valence states in the final product. To our knowledge, no previous reports have investigated the synthesis of phase pure V_2O_3 at atmospheric pressures below 500 °C over a wide temperature range.

Herein, we present a mild approach for synthesizing V_2O_3, a vanadium oxide sensitive to valence states, by employing a new Li vapor-assisted thermal reduction process. The NH_4VO_3 precursor is converted to V_2O_3 using metallic lithium (Li) vapor under N_2 atmosphere conditions at 480 °C, as demonstrated in Scheme 1. All samples obtained are pure in phase and free of impurities, making this mild and rapid process easily scalable. The innovative method can also adjust crystal morphology, size, shape, and internal and surface structures by modifying the synthesis temperature. This high-quality, high-yield V_2O_3 micronanostructure with a customizable crystal structure has varying storage potentials for alkali metal ions, including Li^+, Na^+, and K^+. The samples synthesized between 480 and 680 °C display varying electrochemical performances. This innovative method establishes a straightforward pathway to develop high-quality V_2O_3 and provides a valuable model for the rational design and fundamental understanding of Li^+, Na^+, and K^+ storage mechanisms.

2. EXPERIMENTAL SECTION

2.1. Materials Synthesis. All reagents were procured from Sinopharm Chemical Reagent Co., Ltd. Shanghai, China, and used in analytical grade form without further purification. The synthesis was conducted by using a square-shaped graphite crucible. A Si wafer, serving solely as a substrate, was cleansed with ethyl alcohol and acetone in an ultrasonic cleaner to remove any surface contaminants. Following the cleaning process, the Si wafer was dried and placed on one side of the crucible. Subsequently, 0.234 g (2 mmol) of NH_4VO_3 powder was evenly spread onto the center of the Si wafer. The Si wafer did not participate in the chemical reaction. On the opposite side of the crucible, separate from the Si wafer and NH_4VO_3, a

https://doi.org/10.1021/acsomega.4c03401
ACS Omega 2024, 9, 33815−33825

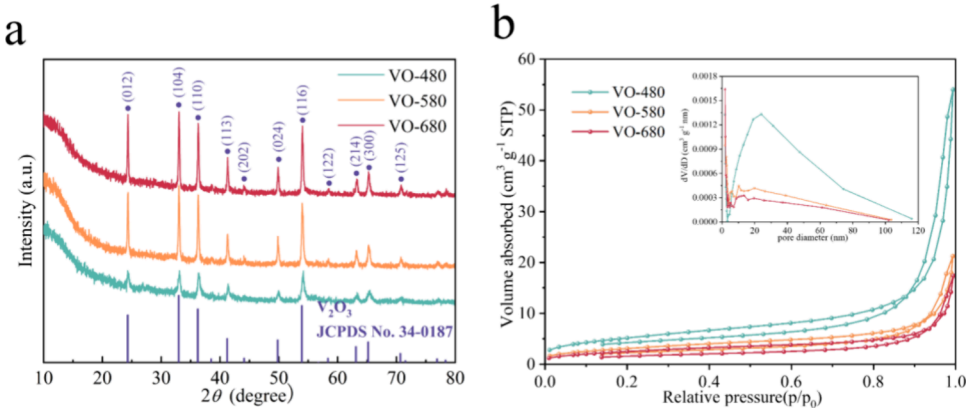

Figure 1. (a) XRD patterns and (b) typical N_2 gas adsorption−desorption isotherms of the as-prepared V_2O_3 samples of VO-480, VO-580, and VO-680. Inset in (b) is the corresponding pore size distribution.

metal Li plate was positioned to function as a reducing agent during the synthesis process.

The crucible containing the Si wafer with NH_4VO_3 and the Li plate was then sealed with a lid. The assembly was heated in a tube furnace to predetermined temperatures of 480, 580, and 680 °C for 2 h under a flowing N_2 atmosphere and subsequently allowed to cool to room temperature naturally. The resulting black powder products were collected at the end of the process. The equation is as follows:

$$x\mathrm{Li} + \mathrm{V_2O_5} \rightarrow \mathrm{V_2O_3} + x\mathrm{Li_2O} \quad (1)$$

where (x) represents the stoichiometry of lithium that interacts with V_2O_5 to yield V_2O_3 and lithium oxide byproduct under the specific conditions of 480 °C in a controlled atmosphere. After the synthesis, we employed an alcohol-washing step to remove any residual lithium oxide (Li_2O) from the product. This ensures that the final material predominantly consists of pure-phase V_2O_3.

The products synthesized at the different calcination temperatures were denoted as VO-480, VO-580, and VO-680. These temperatures were chosen based on the thermal decomposition properties of NH_4VO_3 and the crystal growth requirements of V_2O_3, ensuring that the reaction was completed efficiently within an optimal time frame to yield high-purity and well-controlled crystal phases.[22,23]

2.2. Al_2O_3 Coating on V_2O_3 Electrodes. The V_2O_3 electrodes were prepared by mixing 75 wt % V_2O_3, 15 wt % carbon black, and 10 wt % polyvinylidene fluoride (PVDF) in *N*-methyl-2-pyrrolidinone (NMP). The prepared slurry was then poured onto a copper foil and dried in a vacuum oven at 110 °C for 10 h to evaporate the solvent. The V_2O_3 electrode was used as a substrate for Al_2O_3 thin film deposition using a commercial atomic layer deposition (ALD) reactor (GEMStar XT Atomic Layer Deposition System). Al_2O_3 deposition was performed at 150 °C by sequentially introducing trimethylaluminum (TMA) and H_2O as precursors. Nitrogen was used as the carrier gas at a flow rate of 20 sccm, and the ALD reactor was maintained at a base pressure of typically 200 mTorrs. ALD procedures were set as follows: (1) 21 mSec supply of TMA; (2) 5s extended exposure of TMA to V_2O_3 electrode; (3) 20 s purge of excess TMA and any byproducts; (4) 21 mSec supply of H_2O vapor; (5) 5 s extended exposure of H_2O to V_2O_3 electrode; and (6) 20 s purge of excess H_2O and any byproducts. Using this reaction sequence, the thickness of the Al_2O_3 coating on the V_2O_3 electrode was controlled over 100 ALD cycles. The Al_2O_3 deposition rate was approximately 1 Å per ALD cycle.[24] The VO-480 was used to apply the Al_2O_3 coating with 100 ALD cycles and is about 10 nm thick. The coated sample was named VO-480-ALD.

2.3. Characterization. The crystalline structure of the samples was characterized by powder X-ray diffraction (XRD, D8-Advance X-ray diffractometer, Bruker, Karlsruhe, Germany). Scanning electron microscopy (SEM) was performed on a MIRA3 FEG-SEM (Tescan, Brno, Czech Republic). Transmission electron microscopy (TEM) images were taken with a Hitachi model H-800 instrument. The energy-dispersive X-ray spectra (EDS), high-resolution transmission electron microscopy (HRTEM) images, and electron diffraction (ED) patterns were collected on a JEOL-2010 TEM. Adsorption−desorption analysis was performed on an adsorption instrument (TriStar II 3020).

2.4. Electrochemical Measurements. The CR2032-type button cells were assembled in an Ar-filled glovebox to evaluate the electrochemical performance. The V_2O_3 electrodes or ALD-coated V_2O_3 electrodes were used to construct lithium, sodium, and potassium metal half-cells. The electrolyte for Li-ion batteries was prepared by dissolving 1 M $LiPF_6$ in a mixture of ethylene carbonate (EC) and dimethyl carbonate (DMC) (EC/DMC, 50:50 w/w). One M $NaPF_6$ and 0.8 M KPF6 in EC/DMC were used as electrolytes for sodium-ion and potassium-ion batteries, respectively. The mass load density and the type of separator used for active materials in different batteries are shown in Table S1. The multichannel battery test system (Land CT2001C, Wuhan, China) was used for the charge−discharge cycle test of all cells. Cyclic voltammetry (CV) and electrochemical impedance spectroscopy (EIS) were performed on the Zennium workstation. EIS measurements were also performed in the frequency range of 10 MHz to 100 kHz by applying a potentiostat signal amplitude of 5 mV.

3. RESULTS AND DISCUSSION

The phases of VO-480, VO-580, and VO-680 are characterized by X-ray diffraction (XRD), and the results are shown in Figure 1a. All the diffraction peaks are assigned to the rhombohedral V_2O_3 standard map (JCPDS No. 34-0187), and no other peaks are observed in the XRD patterns, indicating the high purity of the V_2O_3 samples.[25] The global peak height of VO-480 is weaker than those of VO-580 and VO-680, indicating its lowest crystallinity in all samples. The

https://doi.org/10.1021/acsomega.4c03401
ACS Omega 2024, 9, 33815−33825

crystallinity is estimated from the peak areas, while the crystallite size is calculated by Scherrer's equation, and the results are summarized in Table 1. The degree of crystallinity

Table 1. Structure Properties of the As-Prepared Micronano V_2O_3 Particles

sample	crystallinity (%)	crystallite size (nm)	S_{BET} ($m^2\ g^{-1}$)	V_t ($cm^3\ g^{-1}$)[a]	pore size (nm)
VO-480	74.4	24.9	19.1	0.044	24.0
VO-580	81.6	59.3	11.2	0.019	10.3
VO-680	81.3	78.7	9.4	0.015	13.4

[a]The total pore volume of pores at P/P_0 of 0.97.

increases with the reaction temperature for VO-480 and VO-580. After 580 °C, the degree of crystallinity remained essentially unchanged. The crystallite size decreases with the reaction temperature and is 24.9, 59.3, and 78.7 nm for VO-480, VO-580, and VO-680, respectively. The surface area and porous structure of V_2O_3 samples are analyzed using nitrogen adsorption−desorption isotherms, as shown in Figure 1b. All samples show a type IV hysteresis loop, indicating the presence of mesopores (2−50 nm in size). The Brunauer−Emmett−Teller (BET) surface areas are 19.1, 11.2, and 9.4 $m^2\ g^{-1}$ for VO-480, VO-580, and VO-680, respectively. The inset in Figure 1b highlights the pore size distribution and central distributions, which are approximately 24.0, 10.3, and 13.4 nm for VO-480, VO-580, and VO-680, respectively. The Brunauer−Emmett−Teller (BET) surface areas and pore volumes of the as-prepared samples are summarized in Table 1. The large values of BET surface areas and mesopores could provide more reaction sites with fast ion adsorption and short diffusion distance, which may contribute to the fast charge/discharge properties of V_2O_3 samples.

Scanning electron microscopy (SEM) and transmission electron microscopy (TEM) were used to study the morphology and microstructure of the as-prepared V_2O_3 samples. The SEM images in Figure 2a−c show the morphologies of VO-480, VO-580, and VO-680, respectively. The VO-480 consists of particles with an average size of 1−3 μm. The particles are micronano hierarchical structures composed of numerous small, interconnected secondary nanoparticles. As the calcination temperature increases, the particle size of VO-580 becomes smaller, and the hierarchical structures are partially decomposed into nanoparticles of approximately 200−400 nm without secondary grains. In addition, VO-680 consists of almost uniform nanoparticles with an average size of 100−200 nm without hierarchical structures. The TEM images in Figure 2d−f show the internal microstructures of VO-480, VO-580, and VO-680, respectively. In detail, the individual micrometer-scale hierarchical structure of VO-480 in Figure 2d is composed of many nanoparticles without clear boundaries that are closely adjacent.

The TEM image also reveals this unique hierarchical structure in Figure 2g, which shows that the nanoparticles have mesopores with diameters of 3−5 nm. The FFT (fast Fourier transform) of the images of the selected area (red square box) reveals the ring of the (110) plane, with

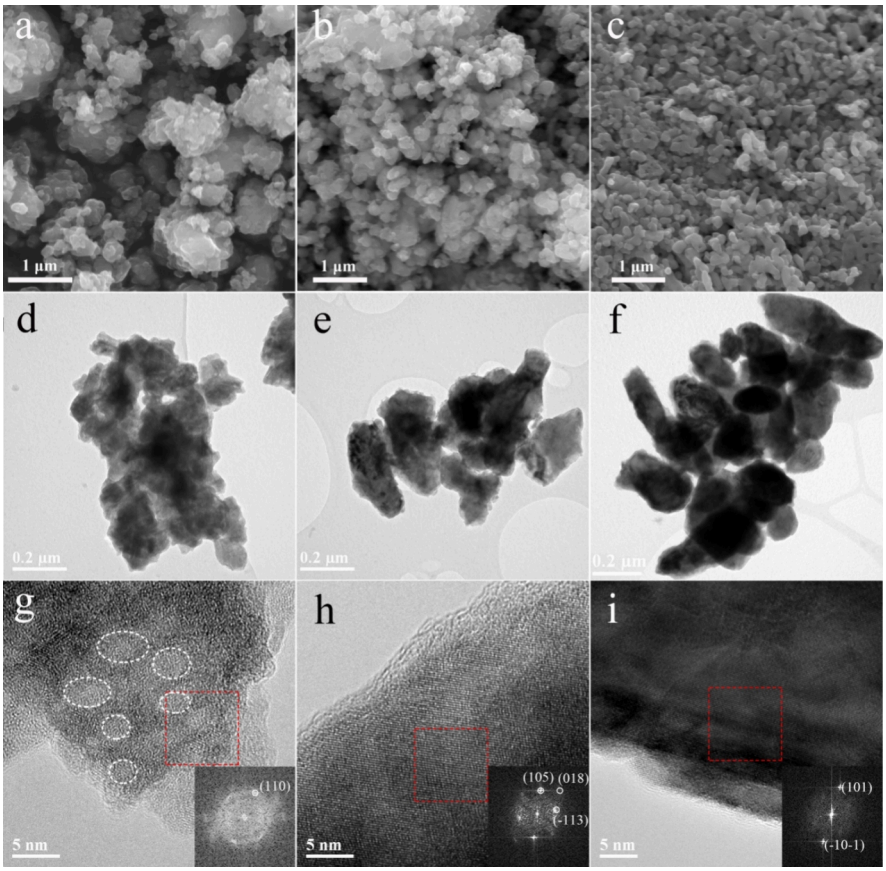

Figure 2. SEM, TEM, and HRTEM images (inset corresponding to obtained FFT images from the red square box of (a,d,g) VO-480, (b,e,h) VO-580, and (c,f,i) VO-680, respectively.

https://doi.org/10.1021/acsomega.4c03401
ACS Omega 2024, 9, 33815−33825

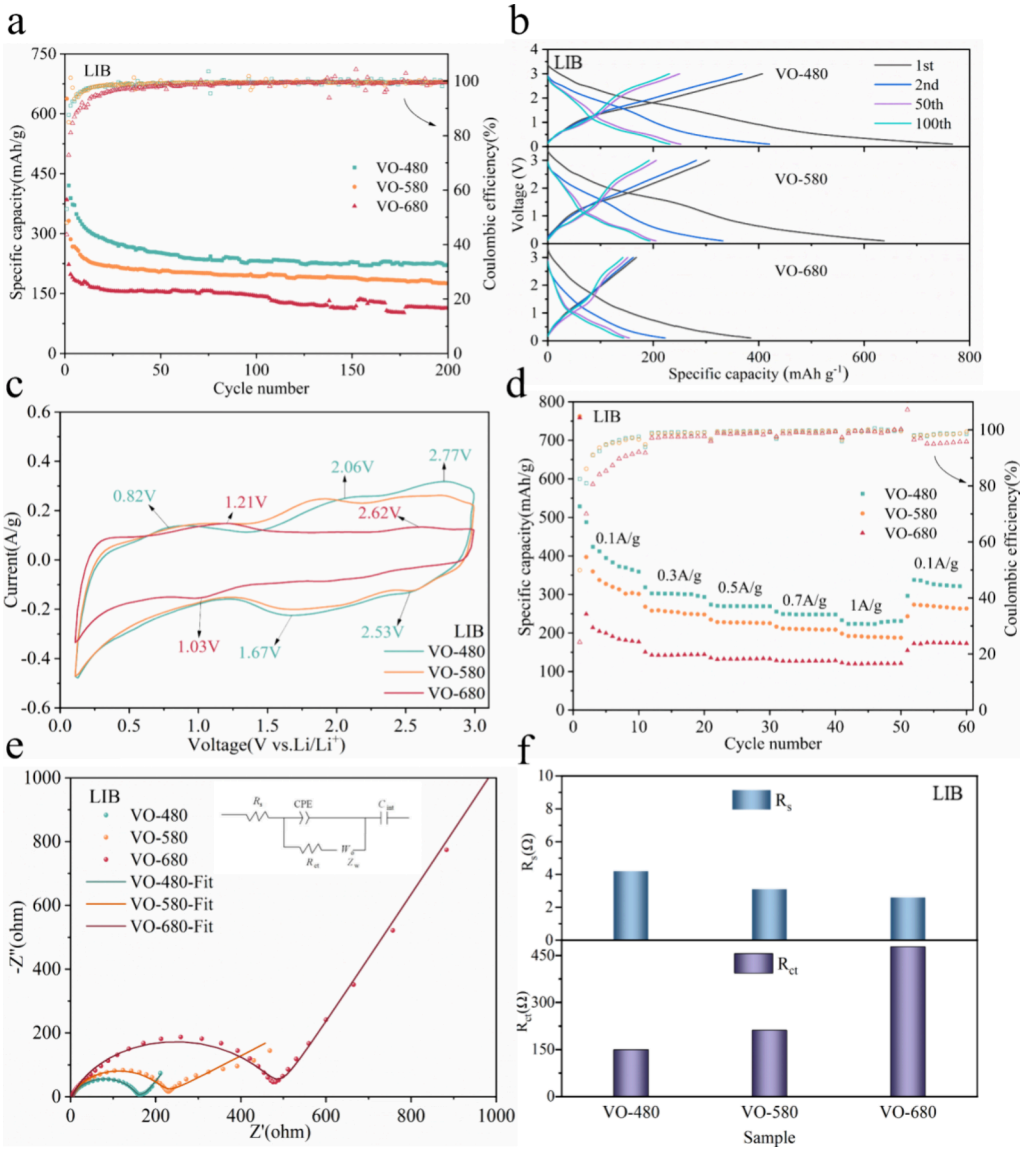

Figure 3. LIBs performance of VO-480, VO-580, and VO-680. (a) Cycling stability, (b) charge−discharge profiles in different cycles, (c) CV curves, (d) rate capability, (e) Nyquist plots (the inset for the equivalent circuit model), and (f) corresponding EIS simulation parameters of R_s and R_{ct}.

interplanar spacings of 0.25 nm matching well for V_2O_3. In contrast, VO-580 are nanoparticles with clear boundaries and diameters of about 200−400 nm. The TEM image in Figure 2h shows that VO-580 has no mesopores. When the synthesis temperature increases to 680 °C, the VO-680 product is all uniform nanoparticles with 100−200 nm diameters. The TEM image in Figure 2i shows their high crystallinity, with no mesoporous structures. These results are consistent with the mesopore size distribution in Figure 1b. VO-480 has a wider mesopore size distribution than VO-580 and VO-680 due to the pore space on the crystal grains.

In Figure S1, the particles within the green circles are primary architectures, while those within the red circles are secondary architectures. The particle sizes of VO-480 and VO-580 are concentrated in the range of 6−12 μm, indicating the presence of secondary architectures. On the other hand, VO-680 has a particle size range of 200−300 nm, confirming that it consists of primary nanoparticles without secondary architectures. Figure 2g−i further validates this observation, and as seen in Figure 2g (within the white dashed box), VO-480 exhibits a more refined mesoporous architecture compared to VO-580.

Compared to the traditional solid-state reaction by reducing gases, Li vapor thermal reduction can easily tune the crystal structures and morphology of the as-prepared V_2O_3 samples by varying the reaction temperature. The VO-480 sample has the largest specific surface area with nano- to mesoscale hierarchical structures compared to VO-580 and VO-680. The tunable structure and surface properties provide an ideal model for investigating alkali metal ion energy storage materials for LIBs, SIBs, and PIBs.

Figure 3 shows the electrochemical performances of VO-480, VO-580, and VO-680 as anode materials for LIBs. Figure 3a shows the cycling performance at 100 mA g^{-1} in 0.01−3 V (vs Li/Li^+). The VO-480 provides a specific discharge capacity of 767 mA h g^{-1} in the first cycle and 420 mA h g^{-1} in the second cycle. The capacity degradation is due to irreversible capacity loss and solid electrolyte interphase (SEI) formation

https://doi.org/10.1021/acsomega.4c03401
ACS Omega 2024, 9, 33815−33825

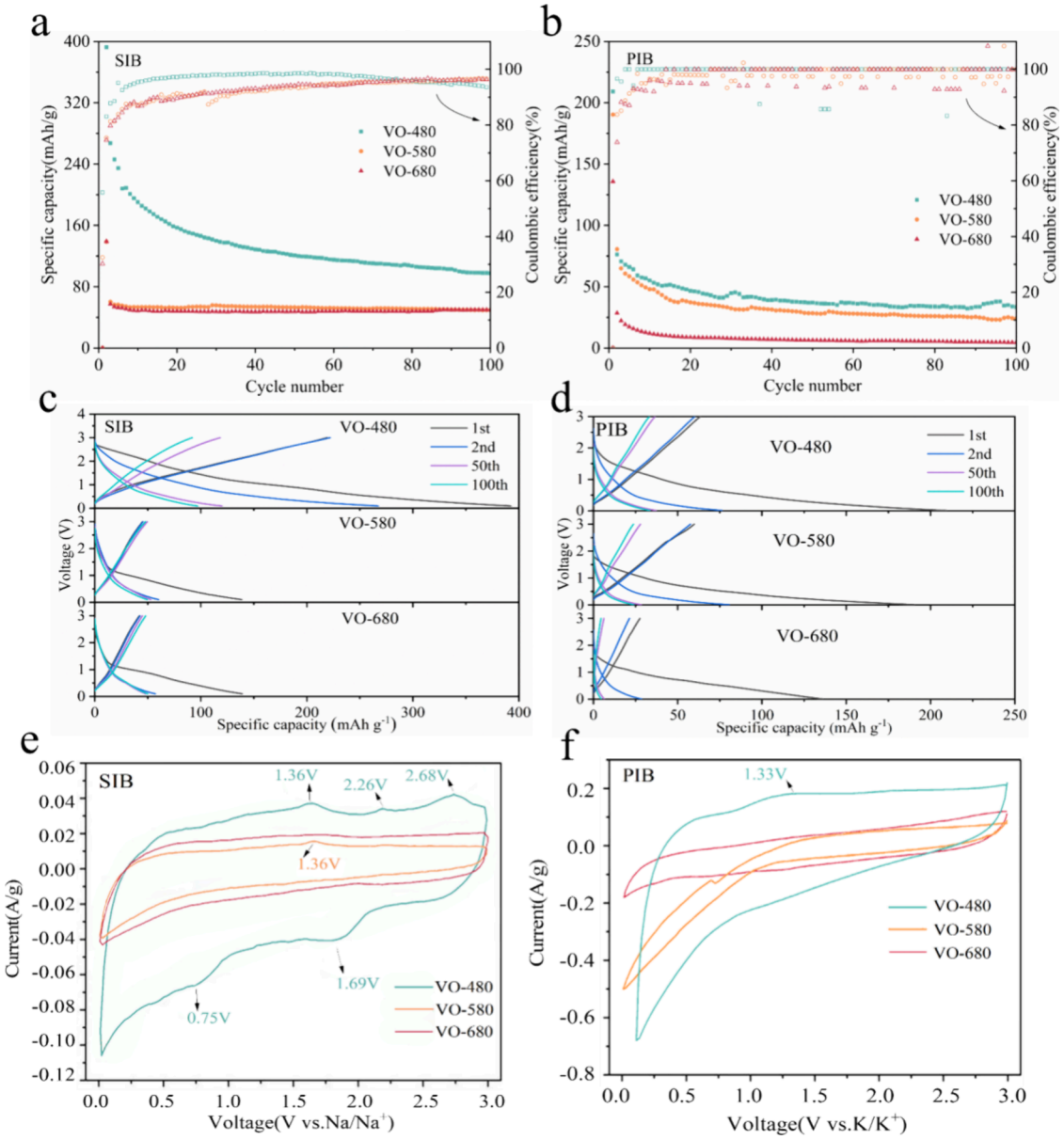

Figure 4. Electrochemical performances of VO-480, VO-580, and VO-680. (a,b) Cycling stability at 100 mA g^{-1}, (c,d) charge−discharge profiles, and (e,f) CV curves for SIBs and PIBs, respectively.

resulting from electrolyte decomposition at the electrode−electrolyte interface. For comparison, VO-580 and VO-680 provide initial specific discharge capacities of 638 and 385 mA h g^{-1}, respectively, and the capacity for the second cycle is 332 and 223 mA h g^{-1}, respectively. After 200 cycles, VO-480 retains a specific discharge capacity of 221 mA h g^{-1}. In contrast, VO-580 and VO-680 provide capacities of 176 and 114 mA h g^{-1}, respectively. The result shows that VO-480 has the highest discharge capacity for LIBs.

Figure 3b displays the charge/discharge profiles for VO-480, VO-580, and VO-680 during the 1st, 2nd, 50th, and 100th cycles. VO-480 and VO-580 exhibit two distinct plateaus at around 2.5 and 1.6 V in the initial discharge curve, indicating the Li^+ insertion reaction in V_2O_3. The minor plateaus below 1.0 V designate the complete reduction to V^0 and Li_2O.[26] These images show both plateaus and sloping regions, indicating a combined potassium storage mechanism involving both intercalation and pseudocapacitive reactions.[27] The sloped curve of VO-680 becomes straight with no plateaus during the charge−discharge process, indicating the structure's destruction. The initial Coulombic efficiencies of VO-480, VO-580, and VO-680 are 53.1, 48.0, and 43.6%, respectively. VO-480 has the highest CE. VO-480 shows the slowest capacity degradation during the 1st, 2nd, 50th, and 100th cycles, indicating its remarkable cycle stability. To address the issue of Coulombic efficiency in the synthesized V_2O_3 electrodes, several strategies have been reported.[25,28,29] These strategies optimize the electrode−electrolyte interface through various surface modification techniques. Such modifications can enhance the stability of the solid electrolyte interface (SEI), improve ion transport, and reduce side reactions, ultimately leading to higher Coulombic efficiency.

The cyclic voltammetric (CV) profiles of the V_2O_3 electrodes at 0.2 mV s^{-1} are shown in Figure 3c. The highly crystallized VO-680 has a reduction peak at about 1.03 V during the first cathodic scan from 3.0 to 0 V, which is

https://doi.org/10.1021/acsomega.4c03401
ACS Omega 2024, 9, 33815−33825

attributed to the reduction of V^{3+} to V^0. However, for the poorly crystallized VO-480, the reduction peaks were at 1.67 and 2.53 V, much higher than that of VO-680. The poor crystallinity of V_2O_3 causes the reduction reaction to occur earlier and more easily. During the anodic scan for VO-680, two peaks at about 1.21 and 2.62 V are attributed to the oxidation reaction.[30] For VO-480, the oxidation peaks were at 0.82, 2.06, and 2.77 V, suggesting a prolonged intercalation process. Meanwhile, the values of the redox peaks for VO-580 are between those of states VO-480 and VO-680. It is worth noting that the extended intercalation process causes the charge−discharge platform to be wider with a large capacity to release. The redox current in VO-480 is much larger than in VO-580 and VO-680, confirming that low crystallinity can promote the electrochemical kinetics of reversible Li^+ insertion and extraction.[31] The different peaks in the CV curves correspond to different reaction states. The electrochemical reaction mechanism of the V_2O_3/CNF electrode likely follows the eqs 2 and 3[32]:

$$V_2O_3 + xLi^+ + Xe^- \leftrightarrow Li_xV_2O_3 \quad (2)$$

$$L_xV_2O_3 + (6 - x)Li^+ + (6 - x)e^- \leftrightarrow 2V + 3Li_2O \quad (3)$$

Figure 3d shows the rate performance of VO-480, VO-580, and VO-680. The VO-480 exhibits specific capacities of 410, 302, 270, 249, and 227 mA h g^{-1} every 10 cycles at current densities of 100, 300, 500, 700, and 1000 mA g^{-1}, respectively. The VO-580 shows 373, 255, 228, 210, and 191 mA h g^{-1}, while the VO-680 shows 254, 144, 133, 127, and 121 mA h g^{-1}. When the current returns to 100 mA g^{-1}, the VO-480 shows a discharge capacity of 324 mA h g^{-1}, much higher than 266 mA h g^{-1} for VO-580 and 172 mA h g^{-1} for VO-680.

To understand the reasons for the improved electrochemical performance of VO-480, electrochemical impedance spectroscopy (EIS) measurements were performed. Figure 3e shows the results obtained and their equivalent circuit, where R_s represents the combination of electrolyte resistance and ohmic resistance of the cell components. R_{ct} and C_{pe} represent the charge transfer resistance between the electrode and the electrolyte and the double-layer capacitance on the electrode surface, respectively. The R_s of all samples are very close to each other, and most R_s are less than 10 Ω. However, the simulated charge transfer resistance (R_{ct}) of VO-480 is 149.4 Ω, which is much lower than those of VO-580 (211.5 Ω) and VO-680 (477.5 Ω). The improvement is mainly due to the coherent porous V_2O_3 framework in VO-480.

Figure 4 shows the electrochemical performance of V_2O_3 as an anode material for SIBs and PIBs. Figure 4a,b shows their cycling performance at 100 mA g^{-1} for SIBs and PIBs, respectively. The VO-480 provides initial specific discharge capacities of 393 and 209 mA h g^{-1} for SIBs and PIBs, respectively. The capacity in the second cycle is 267 and 76 mA h g^{-1}. The capacity gradually decreases and shows a retained capacity of 97 mA h g^{-1} for SIBs and 33 mA h g^{-1} for PIBs on the 100th cycle. In comparison, for SIBs, VO-580 and VO-680 deliver an initial specific discharge capacity of 140 and 139 mA h g^{-1}, and 60 and 57 mA h g^{-1}, respectively, in the second cycle. After 100 cycles, VO-580 and VO-680 deliver a capacity of 50 mA h g^{-1}, half the capacity of VO-480. Meanwhile, for PIBs, VO-580 and VO-680 deliver an initial specific discharge capacity of 190 and 136 mA h g^{-1}, and the capacity for the second cycle is 81 and 29 mA h g^{-1}, respectively. After 100 cycles, VO-580 and VO-680 retain capacities of 24 and 5 mA h g^{-1}, respectively.

The charge/discharge profiles of VO-480, VO-580, and VO-680 in different cycles are compared in Figure 4c,d. For SIBs, all samples show a platform at around 1.1 V in the first discharge curve, which can be attributed to electrolyte decomposition and SEI formation.[33] However, VO-580 and VO-680 show a much sharper slope in the first discharge curve from the open circuit voltage (OCV) to 1.1 V and relatively narrow flat plateaus after 1.1 V, resulting in relatively low capacities. During the next cycle, VO-480 exhibits a slightly decreasing charge/discharge curve, while VO-580 and VO-680 exhibit sharply decreasing curves. This indicates that highly crystallized V_2O_3 is unstable when used for sodium storage. The initial CE values are 55.8, 32.5, and 30.2% for VO-480, VO-580, and VO-680, respectively. VO-480 has the highest CE due to its much lower Na^+ consumption. For PIBs, there is a slight slope in the initial discharge curve from the open circuit voltage to ∼1.1 V. This corresponds to the insertion of K^+ into V_2O_3. In the subsequent discharge curve, a slope with no apparent plateau is related to the extraction of K^+ from $K_xV_2O_3$. In comparison, highly crystalline VO-580 and VO-680 show a sharp slope in the efflux curves. There is only a slight potassiation platform at about 1.1 V. The initial CEs are 30.3, 31.4, and 20.3% for VO-480, VO-580, and VO-680, respectively. The low initial CEs are caused by the strong side reaction between the electrolyte and the electrode surface, resulting in an unstable solid−liquid interface.[34] Additionally, it can be observed that the CE fluctuations in PIBs are more pronounced compared to those in LIBs and SIBs for all three samples. This could be due to the larger ionic radius of K^+ ions, causing more significant structural changes and potential degradation in the electrode material, as well as differences in electrolyte stability and the formation of the solid electrolyte interphase (SEI) layer. The larger size of K^+ ions and their different electrochemical properties can result in a less stable SEI, continuous electrolyte decomposition, and fluctuating CE.

The CV at a scanning rate of 0.2 mV s^{-1} for the first cycle of as-prepared V_2O_3 is shown in Figure 4e,f for SIBs and PIBs, respectively. For SIBs in Figure 4e, the VO-480 exhibits weak cathodic peaks at 1.69 and 0.75 V, corresponding to forming solid electrolyte interphase (SEI) films and the occurrence of the irreversible V^{3+} to $V2^+$ reduction reaction, respectively.[35] In comparison, the peaks at 2.26 and 2.68 V in the first cycle are caused by irreversible oxidation reactions during the Na^+ extraction process.[36,37] The VO-580 shows only one anode peak at 1.36 V and no other redox peaks, indicating pseudocapacitance and intercalation reactions. In addition, the highly crystalline VO-680 shows no redox peaks, expressing a typical capacitive energy storage behavior and agreeing well with the discharge/charge curves.[14,38] All samples for PIBs in Figure 4f describe a typical capacitive behavior with no visible redox peaks and agree well with the discharge/charge curves.[14] Obviously, compared to the electrochemical storage of Li^+, the larger ion radii of Na^+ or K^+ cause difficulty for the intercalation reaction and exhibit more pseudocapacitance reaction with a capacitive feature, resulting in low capacity.

In our study of LIBs, we observed that lithium ions form a comparatively stable SEI layer at the electrode−electrolyte interface due to their relatively small ionic radius. However, as sodium and potassium-ion batteries emerge as alternatives to lithium-ion batteries, the challenges associated with their interfaces in electrochemical storage applications have become

https://doi.org/10.1021/acsomega.4c03401
ACS Omega 2024, 9, 33815−33825

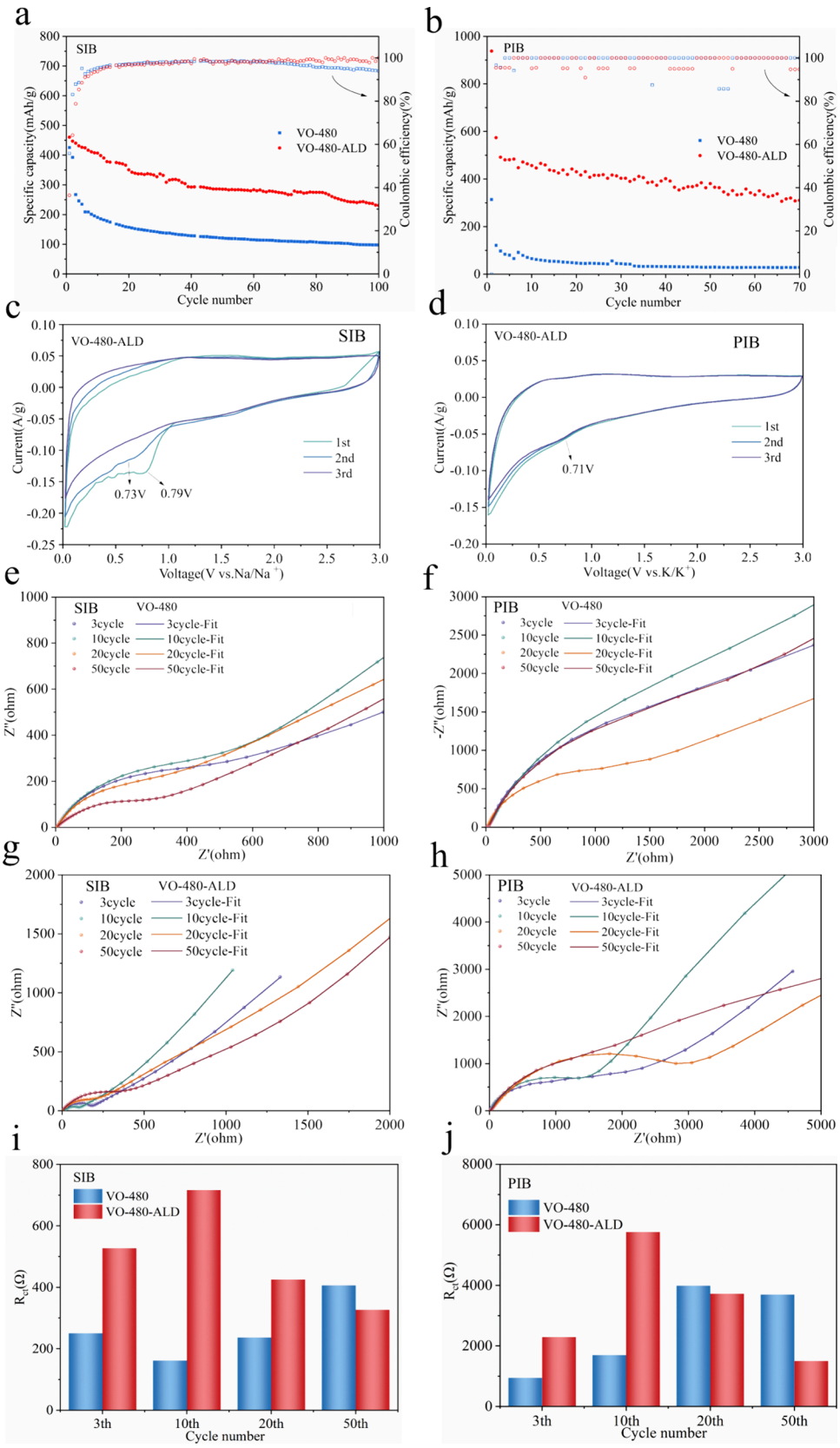

Figure 5. Potassium and sodium storage performance of VO-480 and VO-480-ALD. (a,b) Cycling stability; (c,d) CV curves; (e,f) Nyquist plots for VO-480; (g,h) Nyquist plots for VO-480-ALD; and (i,j) corresponding EIS simulation parameters of R_{ct} for SIBs and PIBs, respectively.

apparent. Mainly, given the larger ionic radius of sodium and potassium ions, the SEI layers at their electrode/electrolyte interfaces are more prone to damage, leading to rapid electrode aging and increasing the charge transfer resistance during battery operation.[7,39,40] Therefore, to overcome these challenges and enhance the battery performance, we decided

https://doi.org/10.1021/acsomega.4c03401
ACS Omega 2024, 9, 33815−33825

to explore advanced modification techniques for the electrode interfaces of sodium and potassium batteries.

Based on these considerations, we employed the ALD method to improve the electrode−electrolyte interface of sodium and potassium batteries. By constructing a stable amorphous Al_2O_3 coating on the VO-480 electrodes, we successfully enhanced the pseudocapacitive response, thereby improving the charge transfer characteristics at the interface. This improvement is particularly crucial for sodium and potassium batteries, as their larger ionic radii make them more susceptible to SEI damage, which is a major contributor to charge transfer resistance. In contrast, while lithium battery technology is relatively mature, enhancing the SEI layer for newer sodium and potassium batteries offers a significant performance advantage. Hence, this research focused on optimizing the interfacial performance of sodium and potassium batteries through ALD technology.

Figure 5a,c,e,g,i illustrates the electrochemical performance of VO-480-ALD as the anode substance for SIBs, and Figure 5b,d,f,h,j exhibits the corresponding outcomes for PIBs. Figure 5a illustrates the cycling performance of the VO-480-ALD for SIBs at a current density of 100 mA g^{-1}. VO-480-ALD displays an initial specific discharge capacity of 447 mA h g^{-1}, higher than the uncoated VO-480, which merely attains 393 mA h g^{-1}. During the second cycle, VO-480-ALD delivers a specific discharge capacitance of 440 mA h g^{-1} as opposed to the capacitance of only 267 mA h g^{-1} attained by VO-480. After 100 cycles, the measured capacity remains stable at 226 mA h g^{-1}, while the VO-480 stands at only 97 mA h g^{-1}. For the PIBs in Figure 5b, VO-480-ALD displays an initial specific discharge capacity of 545 mA h g^{-1}. Furthermore, the capacity for the second cycle reaches 492 mA h g^{-1} and maintains stability at 268 mA h g^{-1} after 100 cycles. The VO-480 electrode for PIBs provides only 209 mA h g^{-1} for the first cycle, 76 mA h g^{-1} for the second cycle, and 33 mA h g^{-1} for the 100th cycle. To better illustrate the morphological changes of VO-480 and VO-480-ALD electrodes before and after cycling, Figure S2 shows SEM images of the pristine morphology of VO-480 and VO-480-ALD electrodes before cycling, and Figure S3 shows SEM images of the morphology of VO-480 and VO-480-ALD electrodes after cycling in PIB. After cycling, it was observed that the VO-480 electrodes exhibited substantial cracks, whereas the VO-480-ALD electrodes, protected by the Al_2O_3 coating, maintained their structural integrity much better. The first three curves of the CV of VO-480-ALD in the voltage range of 0.01−3 V (vs Na/Na^+ and K/K^+) are shown in Figure 5c,d. The additional reduction peaks are observed at 0.79 V for SIBs and 0.71 V for PIBs in the first cycle. These new peaks correspond to the reaction between Al_2O_3 ALD coating and Na^+ or K^+ resources, forming the new artificial SEI, resulting in the formation of K-ion conductive K−Al−O on the surface of the electrode.[15] After that, both third CV cycles express the typical capacitive features without visible redox peaks.

Figure 5e−h displays the Nyquist plots of VO-480-ALD and VO-480 for SIBs and PIBs. The plots depict the high-frequency semicircle, corresponding to the total resistances of the system contact and charge transfer, and the low-frequency region, corresponding to the diffusion process of Na or K into the bulk electrodes. The plots depict the high-frequency semicircle, corresponding to the total resistances of the system contact and charge transfer, and the low-frequency region, corresponding to the diffusion process of Na or K into the bulk electrodes. In Figure 5i, R_{ct} values for VO-480 in SIBs are 250, 161, 236, and 406 Ω for the 3rd, 10th, 20th, and 50th cycles, while for VO-480-ALD, the corresponding values are 527, 716, 425, and 326 Ω, respectively. Before the 20th cycle, the Al_2O_3 coating did not facilitate the transfer of Na^+ on the electrode surface, resulting in a higher R_{ct} of VO-480-ALD. However, in the 10th cycle, the R_{ct} of VO-480-ALD exhibited a decreasing trend and became smaller than that of VO-480. The decline in R_{ct} and the extended cycle indicate that the inert Al_2O_3 coating is transitioning into a conducive artificial SEI. Comparable R_{ct} trends are identifiable for the PIBs in Figure 5j. The R_{ct} values for both VO-480 and VO-480-ALD samples show an increase from the 3rd to the 10th cycle (from 943 to 1692 Ω for VO-480 and from 2286 to 5757 Ω for VO-480-ALD). At the 20th and 50th cycles, the R_{ct} value for VO-480-ALD experiences a sharp decrease, from 3719 to 1499 Ω, while the R_{ct} value for VO-480 remains unchanged, from 3986 to 3695 Ω. Based on the analysis above, the ALD-Al_2O_3 coating effectively reduces the poor cycling performance of the V_2O_3 electrode for Na^+ or K^+ storage by reducing significant charge transfer resistance. This is achieved due to the novel Na^+ or K^+ ion conductive artificial SEI, as KAl_xO_y has been shown to have excellent potassium ion conductivity since it contains partially occupied potassium ion sites.[41] Moreover, after ALD treatment, the V_2O_3 electrode material promotes enhanced interfacial interactions and charge transfer between V_2O_3 and the electrolyte. As a result, the cyclic stability for storing sodium and potassium ions with larger ion radii has improved.

4. CONCLUSIONS

The V_2O_3 micronanostructure was successfully synthesized using Li vapor thermal reduction through a mild process at a relatively low temperature (480 °C). The crystallinity and micronanostructures (lattice disorder, crystallite size, and pore size) of V_2O_3 were easily controlled by the reaction temperature. The micronanostructured V_2O_3 synthesized at 480 °C exhibited the best electrochemical energy storage ability of alkali metal ions (Li^+, Na^+, and K^+). It provided high specific discharge capacities of 767, 393, and 209 mA h g^{-1} for Li^+, Na^+, and K^+ storage, respectively. To minimize the charge transfer resistance caused by the large radii of Na^+ and K^+, an artificial Al_2O_3 SEI layer was deposited by using the ALD method. The Al_2O_3-coated V_2O_3 electrode exhibited a high specific discharge capacity of 447 and 545 mA h g^{-1} for Na^+ and K^+ storage, respectively. The exploration of the ALD technique obviously enhanced the interfacial interaction and charge transfer between V_2O_3 and electrolyte, thus improving the Na^+ and K^+ storage capability. This work is expected to stimulate the exploration of vanadium-based electrodes to realize the exponential growth of sodium and potassium-ion batteries with low cost and high energy density beyond lithium-ion batteries.

■ ASSOCIATED CONTENT

Supporting Information

The Supporting Information is available free of charge at https://pubs.acs.org/doi/10.1021/acsomega.4c03401.

Table S1: mass load density and the type of separator used; Figure S1: particle size distribution; Figure S2: SEM images before cycling; and Figure S3: SEM images after cycling (PDF)

https://doi.org/10.1021/acsomega.4c03401
ACS Omega 2024, 9, 33815−33825

AUTHOR INFORMATION

Corresponding Author

Limei Wang − *Automotive Engineering Research Institute, Jiangsu University, Zhenjiang 212013, China; State Key Laboratory of Intelligent Green Vehicle and Mobility, Tsinghua University, Beijing 100084, China;* orcid.org/0000-0002-8222-9727; Email: wanglimei@ujs.edu.cn

Authors

Liang Liu − *Automotive Engineering Research Institute, Jiangsu University, Zhenjiang 212013, China*

Yichi Zhang − *Automotive Engineering Research Institute, Jiangsu University, Zhenjiang 212013, China*

Yun Wang − *Jiangsu Autoparts New Energy Technology Co., Ltd., Zhenjiang 212132, China*

Jian Liu − *School of Engineering, Faculty of Applied Science, University of British Columbia, Kelowna, BC V1V 1V7, Canada;* orcid.org/0000-0003-0756-2260

Complete contact information is available at: https://pubs.acs.org/10.1021/acsomega.4c03401

Notes

The authors declare no competing financial interest.

ACKNOWLEDGMENTS

This work is supported by the National Natural Science Foundation of China (52072155), the Jiangsu Innovation Support Program for International Science and Technology Cooperation (BZ2023039), the Project of State Key Laboratory of Intelligent Green Vehicle and Mobility (KFY2401), the Science and Technology Plan Project of Zhenjiang (GJ2022010, CZ2023001), and the International Postdoctoral Exchange Fellowship Program (20190078).

REFERENCES

(1) Fouzai, I.; Radaoui, M.; Díaz-Abad, S.; Rodrigo, M. A.; Lobato, J. Electrospray Deposition of Catalyst Layers with Ultralow Pt Loading for Cost-Effective H_2 Production by SO_2 Electrolysis. *ACS Appl. Energy Mater.* **2022**, *5* (2), 2138−2149.

(2) Park, S.; Yoon, N.; Ullah, Z.; Tarus, B. K.; Choi, B.; Kim, H. H.; Son, M. Energy storage capability of seawater batteries for intermittent power generation systems: Conceptualization and modeling. *J. Power Sources* **2023**, *580*, No. 233322.

(3) Wrogemann, J. M.; Haneke, L.; Ramireddy, T.; Frerichs, J. E.; Sultana, I.; Chen, Y. I.; Brink, F.; Hansen, M. R.; Winter, M.; Glushenkov, A. M.; Placke, T. Advanced Dual-Ion Batteries with High-Capacity Negative Electrodes Incorporating Black Phosphorus. *Adv. Sci.* **2022**, *9* (20), No. 2201116.

(4) Sun, D.; Okubo, M.; Yamada, A. Optimal water concentration for aqueous Li intercalation in vanadyl phosphate. *Chem. Sci.* **2021**, *12* (12), 4450−4454.

(5) Savina, A.; Orlova, E.; Morozov, A.; Luchkin, S.; Abakumov, A. Sulfate-Containing Composite Based on Ni-Rich Layered Oxide $LiNi_{0.8}Mn_{0.1}Co_{0.1}O_2$ as High-Performance Cathode Material for Li-ion Batteries. *Nanomaterials* **2020**, *10* (12), 2381.

(6) Song, J.; Wang, H. C.; Zuo, Y. X.; Zhang, K.; Yang, T. H.; Yang, Y. L.; Gao, C.; Chen, T.; Feng, G.; Jiang, Z. W.; Xiao, W. K.; Luo, T.; Xia, D. G. Building Better Full Manganese-Based Cathode Materials for Next-Generation Lithium-Ion Batteries. *Electrochem. Energy Rev.* **2023**, *6* (1), 20.

(7) Min, X.; Xiao, J.; Fang, M. H.; Wang, W.; Zhao, Y. J.; Liu, Y. G.; Abdelkader, A. M.; Xi, K.; Kumar, R. V.; Huang, Z. H. Potassium-ion batteries: outlook on present and future technologies. *Energy Environ. Sci.* **2021**, *14* (4), 2186−2243.

(8) Sada, K.; Darga, J.; Manthiram, A. Challenges and Prospects of Sodium-Ion and Potassium-Ion Batteries for Mass Production. *Adv. Energy Mater.* **2023**, *13* (39), No. 2302321.

(9) Xu, Y.; Zhang, C. L.; Zhou, M.; Fu, Q.; Zhao, C. X.; Wu, M. H.; Lei, Y. Highly nitrogen doped carbon nanofibers with superior rate capability and cyclability for potassium ion batteries. *Nat. Commun.* **2018**, *9*, 1720.

(10) Xu, X. M.; Xiong, F. Y.; Meng, J. S.; Wang, X. P.; Niu, C. J.; An, Q. Y.; Mai, L. Q. Vanadium-Based Nanomaterials: A Promising Family for Emerging Metal-Ion Batteries. *Adv. Funct. Mater.* **2020**, *30* (10), No. 1904398.

(11) Chen, M. Z.; Liu, Q. N.; Hu, Z.; Zhang, Y. Y.; Xing, G. C.; Tang, Y. X.; Chou, S. L. Designing Advanced Vanadium-Based Materials to Achieve Electrochemically Active Multielectron Reactions in Sodium/Potassium-Ion Batteries. *Adv. Energy Mater.* **2020**, *10* (42), No. 2002244.

(12) Petnikota, S.; Toh, J. J.; Li, J. Y.; Chua, R.; Srinivasan, M. Citric Acid Assisted Solid State Synthesis of V_2O_3, V_2O_3/C and V_2O_3/Graphene Composites for Li-ion Battery Anode Applications. *ChemElectroChem.* **2019**, *6* (2), 493−503.

(13) An, X. X.; Yang, H. L.; Wang, Y. P.; Tang, Y.; Liang, S. Q.; Pan, A. Q.; Cao, G. Z. Hydrothermal synthesis of coherent porous V_2O_3/carbon nanocomposites for high-performance lithium-and sodium-ion batteries. *Sci. China-Mater.* **2017**, *60* (8), 717−727.

(14) Yang, L. P.; Zhang, Z. H.; Xia, L. S.; Zhao, Y. F.; Li, F.; Zhang, X.; Wei, J. P.; Zhou, Z. Integrated insights into Na^+ storage mechanism and electrochemical kinetics of ultrafine V_2O_3/S and N co-doped rGO composites as anodes for sodium ion batteries. *J. Mater. Chem. A* **2019**, *7* (39), 22429−22435.

(15) Chen, F.; Wang, S.; He, X. D.; Liao, J. Y.; Hu, Q.; Dong, J. M.; Chen, C. H. Hollow sphere structured V_2O_3@C as an anode material for high capacity potassium-ion batteries. *J. Mater. Chem. A* **2020**, *8* (26), 13261−13266.

(16) Hu, J. X.; Xie, Y. Y.; Zheng, J. Q.; Li, H. Z.; Wang, T. S.; Lai, Y. Q.; Zhang, Z. A. Encapsulating V_2O_3 Nanoparticles in Hierarchical Porous Carbon Nanosheets via C-O-V Bonds for Fast and Durable Potassium-Ion Storage. *ACS Appl. Mater. Interfaces* **2021**, *13* (10), 12149−12158.

(17) Chen, R. J.; Luo, R.; Huang, Y. X.; Wu, F.; Li, L. Advanced High Energy Density Secondary Batteries with Multi-Electron Reaction Materials. *Adv. Sci.* **2016**, *3* (10), No. 1600051.

(18) Sullivan, R. J.; Srinivasan, T. T.; Newnham, R. E. Synthesis of V_2O_3 Powder by Evaporative Decomposition of Solutions and H2 Reduction. *J. Am. Ceram. Soc.* **1990**, *73* (12), 3715−3717.

(19) Kittaka, S.; Sasaki, S.; Morimoto, T. Spherical particles and their surface properties. *J. Mater. Sci.* **1987**, *22* (2), 557−564.

(20) Corr, S. A.; Grossman, M.; Shi, Y.; Heier, K. R.; Stucky, G. D.; Seshadri, R. VO_2(B) nanorods: solvothermal preparation, electrical properties, and conversion to rutile VO2 and V_2O_3. *J. Mater. Chem.* **2009**, *19* (25), 4362−4367.

(21) Ramana, C. V.; Utsunomiya, S.; Ewing, R. C.; Becker, U. Formation of V_2O_3 nanocrystals by thermal reduction of V_2O_5 thin films. *Solid State Commun.* **2006**, *137* (12), 645−649.

(22) Zhang, T.; Zhang, G.; Cao, Z.; Wang, M.; Guan, W.; Wu, S.; Li, Q. Short flow and green process for the production of V_2O_3 powder via ammonia reduction method. *J. Taiwan Inst. Chem. Eng.* **2023**, *151*, No. 105100.

(23) Yang, Z. H.; Cai, P. J.; Chen, L. Y.; Gu, Y. L.; Shi, L.; Zhao, A. W.; Qian, Y. T. A facile route to VN and V_2O_3 nanocrystals from single precursor NH_4VO_3. *J. Alloy. Compd.* **2006**, *420* (1−2), 229−232.

(24) Kaliyappan, K.; Liu, J.; Xiao, B.; Lushington, A.; Li, R.; Sham, T.-K.; Sun, X. Enhanced Performance of P2-$Na_{0.66}(Mn_{0.54}Co_{0.13}Ni_{0.13})O_2$ Cathode for Sodium-Ion Batteries by Ultrathin Metal Oxide Coatings via Atomic Layer Deposition. *Adv. Funct. Mater.* **2017**, *27* (37), No. 1701870.

(25) Jiang, L.; Qu, Y.; Ren, Z. Y.; Yu, P.; Zhao, D. D.; Zhou, W.; Wang, L.; Fu, H. G. *In Situ* Carbon-Coated Yolk-Shell V_2O_3

https://doi.org/10.1021/acsomega.4c03401
ACS Omega 2024, 9, 33815−33825

Microspheres for Lithium-Ion Batteries. *ACS Appl. Mater. Interfaces* **2015**, *7* (3), 1595−1601.
(26) Bai, Y. C.; Tang, Y. K.; Liu, L.; Li, X. H.; Gao, Y. Peapod-like CNT@V_2O_3 with Superior Electrochemical Performance as an Anode for Lithium-Ion Batteries. *ACS Sustain. Chem. Eng.* **2018**, *6* (11), 14614−14620.
(27) Jin, T.; Li, H.; Li, Y.; Jiao, L.; Chen, J. Intercalation pseudocapacitance in flexible and self-standing V_2O_3 porous nanofibers for high-rate and ultra-stable K ion storage. *Nano Energy* **2018**, *50*, 462−467.
(28) Luo, Y.; Ouyang, Z.; Lin, Y.; Song, X.; He, S.; Zhao, J.; Xiao, Y.; Lei, S.; Yuan, C.; Cheng, B. Revealing the synergistic mechanism of multiply nanostructured V_2O_3 hollow nanospheres integrated with doped N, Ni heteroatoms, in-situ grown carbon nanotubes and coated carbon nanolayers for the enhancement of lithium-sulfur batteries. *J. Colloid Interface Sci.* **2022**, *612*, 760−771.
(29) Luo, H.; Wang, B.; Wang, F.; Yang, J.; Wu, F.; Ning, Y.; Zhou, Y.; Wang, D.; Liu, H.; Dou, S. Anodic Oxidation Strategy toward Structure-Optimized V_2O_3 Cathode via Electrolyte Regulation for Zn-Ion Storage. *ACS Nano* **2020**, *14* (6), 7328−7337.
(30) Zhang, D.; Li, G. S.; Li, B. Y.; Fan, J. M.; Liu, X. Q.; Chen, D. D.; Li, L. P. A facile strategy to fabricate V_2O_3/Porous N-doped carbon nanosheet framework as high-performance anode for lithium-ion batteries. *J. Alloy. Compd.* **2019**, *789*, 288−294.
(31) Zhang, T.; Zhang, L.; Zhao, L. N.; Huang, X. X.; Li, W.; Li, T.; Shen, T.; Sun, S. N.; Hou, Y. L. Free-Standing, Foldable V_2O_3/Multichannel Carbon Nanofibers Electrode for Flexible Li-Ion Batteries with Ultralong Lifespan. *Small* **2020**, *16* (47), No. 2005302.
(32) Liu, X.; Liu, R.; Zeng, L.; Huang, X.; Chen, X.; Zheng, C.; Xu, Y.; Qian, Q.; Wei, M.; Chen, Q. Facile preparation of a V_2O_3/carbon fiber composite and its application for long-term performance lithium-ion batteries. *New J. Chem.* **2017**, *41* (13), 5380−5386.
(33) Ren, Q. Y.; Qin, N.; Liu, B.; Yao, Y.; Zhao, X.; Deng, Z.; Li, Y.; Dong, Y. C.; Qian, D.; Su, B. L.; Zhang, W. J.; Wang, H. E. An oxygen-deficient vanadium oxide@N-doped carbon heterostructure for sodium-ion batteries: insights into the charge storage mechanism and enhanced reaction kinetics. *J. Mater. Chem. A* **2020**, *8* (6), 3450−3458.
(34) Liu, Y. W.; Gao, C.; Dai, L.; Deng, Q. B.; Wang, L.; Luo, J. Y.; Liu, S.; Hu, N. The Features and Progress of Electrolyte for Potassium Ion Batteries. *Small* **2020**, *16* (44), No. 2004096.
(35) Li, Y. T.; Zhang, S.; Wang, S. T.; Leng, J.; Jiang, C. H.; Ren, X. W.; Zhang, Z. T.; Yang, Y.; Tang, Z. L. A multi-shelled V_2O_3/C composite with an overall coupled carbon scaffold enabling ultrafast and stable lithium/sodium storage. *J. Mater. Chem. A* **2019**, *7* (33), 19234−19240.
(36) Sarkar, A.; Sinha, A. K.; Mitra, S. Nanostructured vanadium trioxides, as a long life and high performance anode for sodium-ion battery. *Electrochim. Acta* **2019**, *299*, 914−925.
(37) Yao, J. X.; Zhang, H.; Zhao, Z. J.; Zhu, Z. X.; Yao, J. L.; Zheng, X. Y.; Yang, Y. Melamine-assisted synthesis of porous V_2O_3/N-doped carbon hollow nanospheres for efficient sodium-ion storage. *Dalton Trans.* **2021**, *50* (11), 3867−3873.
(38) Zhang, J. B.; Li, Q. W.; Liao, Z. H.; Wang, L.; Xu, J.; Ren, X. C.; Gao, B. A.; Chu, P. K.; Huo, K. F. In situ Synthesis of V_2O_3-Intercalated N-doped Graphene Nanobelts from VO_x-Amine Hybrid as High-Performance Anode Material for Alkali-Ion Batteries. *ChemElectroChem.* **2018**, *5* (10), 1387−1393.
(39) Vardar, G.; Bowman, W. J.; Lu, Q. Y.; Wang, J. Y.; Chater, R. J.; Aguadero, A.; Seibert, R.; Terry, J.; Hunt, A.; Waluyo, I.; Fong, D. D.; Jarry, A.; Crumlin, E. J.; Hellstrom, S. L.; Chiang, Y. M.; Yildiz, B. Structure, Chemistry, and Charge Transfer Resistance of the Interface between $Li_7La_3Zr_2O_{12}$ Electrolyte and $LiCoO_2$ Cathode. *Chem. Mater.* **2018**, *30* (18), 6259−6276.
(40) Ma, M.; Pan, H.; Hu, Y. Progress in electrolyte research for non-aqueous sodium ion batteries. *Energy Storage Sci. Technol.* **2020**, *9* (5), 1234−1250.
(41) Zhang, Y.; Zhu, H. Z.; Freschi, D. J.; Liu, J. High-Performance Potassium-Tellurium Batteries Stabilized by Interface Engineering. *Small* **2022**, *18* (15), No. 2200085.

https://doi.org/10.1021/acsomega.4c03401
ACS Omega 2024, 9, 33815−33825